



Topological resonance in Weyl semimetals in a circularly polarized optical pulse

Fatemeh Nematollahi , S. Azar Oliaei Motlagh, Jhih-Sheng Wu, Rupesh Ghimire , Vadym Apalkov, and Mark I. Stockman
Center for Nano-Optics (CeNO) and Department of Physics and Astronomy, Georgia State University, Atlanta, Georgia 30303, USA



(Received 8 April 2020; revised 17 August 2020; accepted 27 August 2020; published 9 September 2020)

We study theoretically the ultrafast electron dynamics of three-dimensional Weyl semimetals in the field of a laser pulse. For a circularly polarized pulse, such dynamics is governed by topological resonance, which manifests itself as a specific conduction band population distribution in the vicinity of the Weyl points. The topological resonance is determined by the competition between the topological phase and the dynamic phase and depends on the handedness of a circularly polarized pulse. Also, we show that the conduction band population induced by a circularly polarized pulse that consists of two oscillations with opposite handedness is highly chiral, which represents the intrinsic chirality of the Weyl points.

DOI: [10.1103/PhysRevB.102.125413](https://doi.org/10.1103/PhysRevB.102.125413)

I. INTRODUCTION

The interaction of ultrafast laser pulses with solids was a subject of intensive theoretical and experimental research over the last two decades. Such interaction is characterized by highly nonlinear electron dynamics and strong perturbation of electron systems and can be used to probe and control the transport and optical properties of solids within a femtosecond timescale [1–6]. The ultrafast electron dynamics in the field of the pulse is determined by electron energy dispersion and interband dipole matrix elements. Such matrix elements strongly depend on the topology of the system and have singularities in the reciprocal space for topologically nontrivial solids. Such singularities strongly modify ultrafast electron dynamics and result in unique features in both electron population of the conduction band and generated electric currents. One of the materials with nontrivial topology is a two-dimensional (2D) graphene monolayer, which belongs to the class of Dirac semimetals that have linear energy dispersion near special points called the Dirac points [7].

Graphene is a unique material, which has amazing electrical, optical, and mechanical properties as well as numerous potential applications [8,9]. Graphene is a single layer of carbon atoms with a honeycomb crystal structure that has two inequivalent Dirac points (\mathbf{K} and \mathbf{K}') in the first Brillouin zone. These two Dirac points have nonzero Berry flux of opposite signs, which makes graphene a locally topologically nontrivial material, while the total Berry flux through the whole Brillouin zone is zero. While in graphene, the relativistic energy dispersion and nonzero Berry flux at the Dirac points are realized in 2D, the corresponding Dirac points can be also realized in three-dimensional (3D) solids, i.e., in Dirac semimetals. In 3D, the Dirac points are double degenerate. Such degeneracy is protected by time-reversal and inversion symmetries of the solid. To lift the degeneracy, either time-reversal symmetry \mathcal{T} [10] or inversion symmetry \mathcal{P} [11] should be broken. In this case the Dirac point is transformed into a set of separated Weyl points, which are monopoles of

Berry curvature. Such materials are called Weyl semimetals. Due to the fermion doubling theorem [12], the Weyl points appear in pairs with opposite chiralities, i.e., the Weyl points in a pair are sink or source of the Berry curvature.

Recent studies have revealed that Weyl semimetals show strong nonlinear optical response such as the second harmonic generation (SHG) [13] and nonlinear Hall effect [14]. These nonlinear effects are of topological origin and are due to large Berry curvature localized near the Weyl points. Furthermore, a circularly polarized pulse can excite electrons near the Weyl points selectively [15,16]. Such selectivity can open new opportunities for device applications.

The response of the Weyl semimetals to a linearly polarized ultrafast pulse has been studied theoretically in Ref. [17]. The results show that the electron dynamics in such materials is coherent and highly anisotropic. At the same time, in Refs. [5,18] it was shown that the response of a solid to a circularly polarized ultrashort pulse can have some extra features. Namely, for gapped graphenelike materials, such as transition metal dichalcogenides, the electrons experience topological resonance in the field of circularly polarized pulse, while there is no such resonance for linearly polarized pulse. The topological resonance occurs due to competition between the topological phase and the dynamic phase and results in predominant population of one of the valleys of graphenelike materials. The topological resonance occurs only for gapped graphene materials but not for pristine graphene and strongly depends on the magnitude of the band gap. In this relation the Weyl semimetal becomes an interesting system to study the topological resonance since near each Weyl point, in the reciprocal space, the 2D cross sections are equivalent to gapped graphene systems with the band gap that depends on the distance of the 2D cross section to the Weyl point. Thus, by studying the interaction of Weyl semimetals with circularly polarized pulse we can study the ultrafast electron dynamics for both pristine graphene and gapped graphene with different band gaps. In this paper, we consider the interaction of Weyl semimetals with ultrafast circularly polarized pulses of

different handedness. We identify the features of topological resonance in the conduction band population distribution in the reciprocal space of Weyl semimetal.

II. MODEL AND EQUATIONS

In the presence of an external electric field, the full Hamiltonian of the system becomes

$$H(t) = H_0 + e\mathbf{F}(t)\mathbf{r}, \quad (1)$$

where e is the electron charge and H_0 is the field-free Hamiltonian of the system. For the field-free Hamiltonian we use the two-band model of Weyl semimetals. Such Hamiltonian H_0 describes the low-energy excitations near two Weyl points located at $k_w^\pm = (\pm k_0, 0, 0)$ in the reciprocal space. Below we will mainly consider type I Weyl semimetals, for which there is a well-pronounced topological resonance. The Hamiltonian of the type I Weyl semimetals has the following form [19]:

$$\mathcal{H}_0(\mathbf{k}) = A(\mathbf{k})\sigma_x + B(\mathbf{k})\sigma_y + C(\mathbf{k})\sigma_z, \quad (2)$$

where $\mathbf{k} = (k_x, k_y, k_z)$ is a vector of the reciprocal space, $\sigma_x, \sigma_y, \sigma_z$ are Pauli matrices, and $A(\mathbf{k}), B(\mathbf{k}), C(\mathbf{k})$ are given by the expressions

$$\begin{aligned} A(\mathbf{k}) &= t_x[\cos(k_x a) - \cos(k_0 a)] \\ &\quad + t_y[\cos(k_y b) - 1] + t_z[\cos(k_z c) - 1], \\ B(\mathbf{k}) &= t_y \sin(k_y b), \quad C(\mathbf{k}) = t_z \sin(k_z c). \end{aligned} \quad (3)$$

Here, a, b , and c are lattice constants along x, y , and z directions, respectively, and t_x, t_y, t_z are hopping integrals which are related to the Fermi velocities v_x, v_y , and v_z at the Weyl points through the following expressions:

$$v_x = -(a/\hbar)t_x \sin(\pm k_0 a), \quad v_y = (b/\hbar)t_y, \quad v_z = (c/\hbar)t_z. \quad (4)$$

First, we apply our analysis to TaAs (Weyl semimetal type I), which has a body-centered tetragonal lattice system, with lattice constants $a = b = 3.437 \text{ \AA}$ along x and y directions, respectively, and $c = 11.646 \text{ \AA}$ along z direction. The space group in TaAs is $I4_1md$ (No. 109, C_{4v}) [20]. The important symmetries are the time-reversal symmetry (\mathcal{T}), the fourfold-rotational symmetry around the \hat{z} axis (C_{4z}), and two mirror reflections about $x = 0$ and $y = 0$. TaAs has 24 Weyl points: 8 Weyl points are located at $(\pm 0.0072\pi/a, 0.4827\pi/b, 1.000\pi/c)$ and are called W_1 and 16 Weyl points are located at $(\pm 0.0185\pi/a, 0.2831\pi/b, 0.6000\pi/c)$ and are called W_2 [21,22]. The two-band Hamiltonian (2) is used to describe the electron dynamics near one pair of Weyl points. Below we consider the Weyl points that are located at $(\pm 0.1, 0, 0)$. The hopping integrals are $t_x = 1.8801 \text{ eV}$, $t_y = 0.4917 \text{ eV}$, and $t_z = 0.1646 \text{ eV}$. The energy dispersion of TaAs near the Weyl points as a function of k_x and k_y and at $k_z = 0$ is shown in Fig. 1.

We assume that during the pulse the electron dynamics is coherent and is described by the time-dependent Schrödinger equation (TDSE)

$$i\hbar \frac{d\Psi}{dt} = \hat{H}(t)\Psi. \quad (5)$$

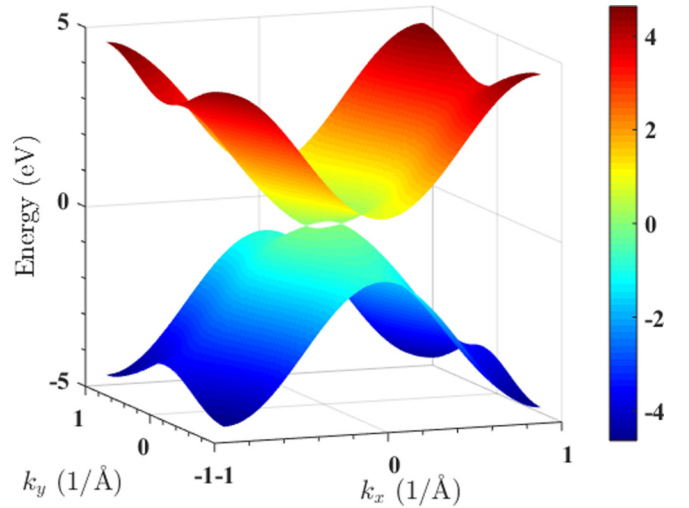


FIG. 1. Energy dispersion of TaAs as a function of k_x and k_y at $k_z = 0$.

The electric field of the pulse generates both interband and intraband electron dynamics. The intraband dynamics is determined by the Bloch acceleration theorem [23]

$$\hbar \frac{d\mathbf{k}}{dt} = e\mathbf{F}(t), \quad (6)$$

solution of which has the form

$$\mathbf{k}(\mathbf{q}, t) = \mathbf{q} + \frac{e}{\hbar} \int_{-\infty}^t \mathbf{F}(t') dt', \quad (7)$$

where \mathbf{q} is the initial electron wave vector.

The corresponding wave functions, which are solutions of the time-dependent Schrödinger equation within a single band, are Houston functions [24] and are given by the expression

$$\Phi_{\alpha\mathbf{q}}^{(H)}(\mathbf{r}, t) = \Psi_{\mathbf{k}(\mathbf{q}, t)}^{(\alpha)}(\mathbf{r}) \exp(i\phi_{\alpha}^{(D)}(\mathbf{q}, t) + i\phi_{\alpha}^{(B)}(\mathbf{q}, t)), \quad (8)$$

where $\Psi_{\mathbf{k}}^{(\alpha)}(\mathbf{r})$ are Bloch wave functions with wave vector \mathbf{k} at band α , $\alpha = v$ for the valence band, and $\alpha = c$ for the conduction band. The dynamic phase $\phi_{\alpha}^{(D)}$ and the geometric (Berry) phase $\phi_{\alpha}^{(B)}$ are defined by the following expressions:

$$\phi_{\alpha}^{(D)}(\mathbf{q}, t) = -\frac{1}{\hbar} \int_{-\infty}^t dt' E_{\alpha}[\mathbf{k}(\mathbf{q}, t')], \quad (9)$$

$$\phi_{\alpha}^{(B)}(\mathbf{q}, t) = \frac{e}{\hbar} \int_{-\infty}^t dt' \mathbf{F}(t') \mathbf{A}^{\alpha\alpha}[\mathbf{k}(\mathbf{q}, t')], \quad (10)$$

where $\mathbf{A}^{\alpha\alpha} = \langle \Psi_{\mathbf{q}}^{(\alpha)} | i \frac{\partial}{\partial \mathbf{q}} | \Psi_{\mathbf{q}}^{(\alpha)} \rangle$ is the intraband Berry connection for band α .

It is convenient to express the solution of TDSE (5) in the basis of Houston functions as

$$\Psi_{\mathbf{k}(\mathbf{q}, t)}^{(\alpha)}(\mathbf{r}) = \sum_{\alpha=v,c} \beta_{\alpha\mathbf{q}}(t) \Phi_{\alpha\mathbf{q}}^{(H)}(\mathbf{r}, t), \quad (11)$$

where $\beta_{\alpha\mathbf{q}}(t)$ are expansion coefficients. These coefficients satisfy the following system of equations:

$$i\hbar \frac{\partial B_{\mathbf{q}}(t)}{\partial t} = H'(\mathbf{q}, t) B_{\mathbf{q}}(t), \quad (12)$$

where $B_q(t)$ and Hamiltonian $H'(\mathbf{q}, t)$ are defined as

$$B_q(t) = \begin{pmatrix} \beta_{v,q}(t) \\ \beta_{c,q}(t) \end{pmatrix} \quad (13)$$

and

$$H'(\mathbf{q}, t) = e\mathbf{F}(t)\hat{\mathbf{A}}(\mathbf{q}, t), \quad (14)$$

where

$$\hat{\mathbf{A}}(\mathbf{q}, t) = \begin{bmatrix} 0 & \mathcal{D}^{cv}(\mathbf{q}, t) \\ \mathcal{D}^{vc}(\mathbf{q}, t) & 0 \end{bmatrix}, \quad (15)$$

$$\mathcal{D}^{cv}(\mathbf{q}, t) = \mathbf{A}^{cv}[\mathbf{k}(\mathbf{q}, t)] \exp[i(\phi_{cv}^{(B)}(\mathbf{q}, t) + \phi_{cv}^{(D)}(\mathbf{q}, t))], \quad (16)$$

$$\phi_{cv}^{(D)}(\mathbf{q}, t) = \phi_v^{(D)}(\mathbf{q}, t) - \phi_c^{(D)}(\mathbf{q}, t), \quad (17)$$

$$\phi_{cv}^{(B)}(\mathbf{q}, t) = \phi_v^{(B)}(\mathbf{q}, t) - \phi_c^{(B)}(\mathbf{q}, t). \quad (18)$$

Here, $\phi_{cv}^{(D)}(\mathbf{q}, t)$ is a dynamic phase, $\phi_{cv}^{(B)}(t)$ is a topological phase, and matrix $\mathbf{A}_{cv}(\mathbf{k})$ is the non-Abelian k -space gauge potential called Berry connection and expressed as [25,26]

$$\mathbf{A}^{cv}(\mathbf{q}) = \langle \Psi_{\mathbf{q}}^{(c)} | i \frac{\partial}{\partial \mathbf{q}} | \Psi_{\mathbf{q}}^{(v)} \rangle, \quad (19)$$

which can be found analytically in the case of type I Weyl semimetals as

$$\begin{aligned} \mathbf{A}_x^{vc} &= (\mathbf{A}_x^{cv})^* = \frac{t_x a}{2i(A^2(\mathbf{k}) + B^2(\mathbf{k}) + C^2(\mathbf{k}))} \\ &\times \frac{\sin(k_x a)}{\sqrt{A^2(\mathbf{k}) + B^2(\mathbf{k})}} \\ &\times [A(\mathbf{k})C(\mathbf{k}) - iB(\mathbf{k})\sqrt{A^2(\mathbf{k}) + B^2(\mathbf{k}) + C^2(\mathbf{k})}], \end{aligned} \quad (20)$$

$$\begin{aligned} \mathbf{A}_y^{vc} &= (\mathbf{A}_y^{cv})^* = \frac{t_y a}{2i(A^2(\mathbf{k}) + B^2(\mathbf{k}) + C^2(\mathbf{k}))} \\ &\times \frac{1}{\sqrt{A^2(\mathbf{k}) + B^2(\mathbf{k})}} [C(\mathbf{k})(A(\mathbf{k}) \sin(k_y a) \\ &- B(\mathbf{k}) \cos(k_y a)) - i\sqrt{A^2(\mathbf{k}) + B^2(\mathbf{k}) + C^2(\mathbf{k})} \\ &\times (A(\mathbf{k}) \cos(k_y a) + B(\mathbf{k}) \sin(k_y a))], \end{aligned} \quad (21)$$

$$\begin{aligned} \mathbf{A}_z^{vc} &= (\mathbf{A}_z^{cv})^* = \frac{t_z c \sqrt{A^2(\mathbf{k}) + B^2(\mathbf{k})}}{2i(A^2(\mathbf{k}) + B^2(\mathbf{k}) + C^2(\mathbf{k}))} \\ &\times \left[\cos(k_z c) + \frac{\sin(k_z c)}{A^2(\mathbf{k}) + B^2(\mathbf{k})} \right. \\ &\times (A(\mathbf{k})C(\mathbf{k}) - iB(\mathbf{k})\sqrt{A^2(\mathbf{k}) + B^2(\mathbf{k}) + C^2(\mathbf{k})}) \left. \right]. \end{aligned} \quad (22)$$

We numerically solve differential equation (12) with initial conditions $(\beta_{vq}, \beta_{cq}) = (1, 0)$. A general solution can be expressed in terms of the evolution operator $\hat{U}(\mathbf{q}, t)$ as

$$B_q(t) = \hat{U}(\mathbf{q}, t) B_q(-\infty), \quad (23)$$

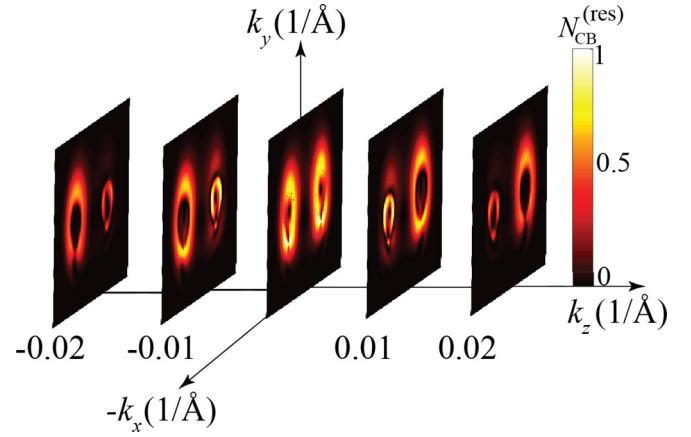


FIG. 2. Residual CB population distribution as a function of (k_x, k_y) for different values of k_z after a single-oscillation left-handed circularly polarized pulse. The pulse with the field amplitude of $F_0 = 3 \text{ mV/\AA}$ propagates along the z direction.

$$\hat{U}(\mathbf{q}, t) = \hat{T} \exp \left[i \int_{t'=-\infty}^t \hat{\mathbf{A}}(\mathbf{q}, t') d\mathbf{k}(\mathbf{q}, t') \right], \quad (24)$$

where \hat{T} denotes the time-ordering operator and the integral is affected along the Bloch trajectory $\mathbf{k}(\mathbf{q}, t)$. We characterize the electron dynamics in terms of the conduction band population distribution $N_{CB}(\mathbf{q}, t) = |\beta_{cq}(t)|^2$ in the reciprocal space.

III. RESULTS AND DISCUSSION

The rest of the paper is organized as follows: In the Sec. III A we consider a circularly polarized pulse propagating along the z direction. We characterize the electron dynamics in the field of the pulse by the residual conduction band (CB) population distribution in the reciprocal space. The data show that a circularly polarized single oscillation pulse induces the topological resonance in the system. In Sec. III B we apply a circularly polarized pulse that consists of two cycles. The optical pulse propagates in the z direction and induces a CB population distribution in the reciprocal space, which is highly chiral and shows the chirality of the Weyl points.

A. A single-oscillation circularly polarized pulse

1. Type I Weyl semimetals

We study the response of Weyl semimetals type I to a single-oscillation circularly polarized pulse in terms of residual CB population in the reciprocal space. We assume that the left-handed circularly polarized optical pulse propagates along the z direction and its components are defined as

$$F_x(t) = -F_0 e^{-u^2} (1 - 2u^2), \quad \text{quad } F_y(t) = 2u F_0 e^{-u^2}, \quad (25)$$

where the field amplitude $F_0 = 3 \text{ mV/\AA}$, $u = t/\tau$, and $\tau = 10 \text{ fs}$ is the pulse duration. We numerically solve TDSE [see Eq. (12)], with initial condition $(\beta_{vq}, \beta_{cq}) = (1, 0)$. Applied optical field causes redistribution of electrons between the valence and conduction bands, which results in finite CB population. The residual CB population, i.e., the CB population at the end of the pulse, $t = 25 \text{ fs}$, is shown in Fig. 2.

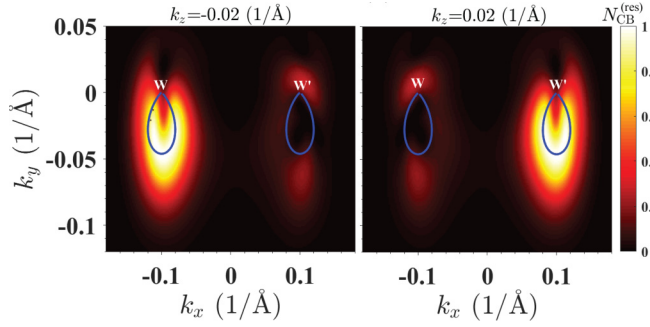


FIG. 3. Residual CB population distribution in the reciprocal space as a function of (k_x, k_y) for $k_z = \pm 0.2$ ($1/\text{\AA}$) after a single-oscillation left-handed circularly polarized pulse. The pulse with the field amplitude $F_0 = 3$ mV/ \AA propagates along the z direction. The separatrix is shown by a solid blue line.

At $k_z = 0$, the electron system in the (k_x, k_y) plane is equivalent to pristine graphene and the responses at both Weyl points to an external electric field are similar. The corresponding CB population distribution is symmetric with respect to y axes. The large CB population is located near the Weyl points (see Fig. 2), which correlates with the profile of the interband dipole coupling that is the strongest near the Weyl points. This property is similar to what we have in graphene [27] and is due to singularity of the dipole coupling exactly at the Weyl points or Dirac points for graphene. Since the interband dipole matrix elements are highly localized near the Weyl points, the conduction band population distribution has sharp maxima along the separatrix (solid blue line in Fig. 3). Here, the separatrix is defined as a set of points in the reciprocal space, for which the electron trajectory during the pulse goes directly through the Weyl point.

For a nonzero value of k_z , the electron system in the k_x - k_y plane, near each Weyl point, becomes similar to gapped graphene [18] with the band gap that is proportional to $|k_z|$. The corresponding CB population distribution as a function of k_x and k_y and for different k_z is shown in Fig. 2. The data show that for nonzero k_z , the W , $(-0.1, 0, 0)$, and W' , $(0.1, 0, 0)$, points are populated differently. For $k_z > 0$, the CB is highly populated in the vicinity of W' point, while it is less populated for $k_z < 0$. This is different from the CB population distribution for $k_z = 0$ and is due to the fact that for $k_z \neq 0$, the effective 2D system (in k_x - k_y plane) becomes similar to gapped graphene, for which there is the effect of topological resonance. The origin of the topological resonance can be understood by looking at the expression for the CB population in the first order of the perturbation theory. Namely, within this approximation, the CB population is given by the expression

$$n_{CB} = \left| \oint |\mathcal{A}_{cv}[\mathbf{k}(\mathbf{q}, t)]\mathbf{n}(t)| \exp(i\phi_{cv}^{(tot)}(\mathbf{q}, t)) d\mathbf{k}(\mathbf{q}, t) \right|^2, \quad (26)$$

where $\mathbf{n}(t) = \mathbf{F}(t)/F(t)$ is the unit vector tangential to the Bloch trajectory and the total phase $\phi^{(tot)}$ is

$$\phi_{cv}^{(tot)} = \phi_{cv}^{(B)}(\mathbf{q}, t) + \phi_{cv}^{(A)}(\mathbf{q}, t) + \phi_{cv}^{(D)}(\mathbf{q}, t), \quad (27)$$

where the dipole matrix element phase $\phi_{cv}^{(A)}(\mathbf{q}, t)$ is defined as

$$\phi_{cv}^{(A)}(\mathbf{q}, t) = \arg(\mathcal{A}_{cv}(\mathbf{k}(\mathbf{q}, t)\mathbf{n}(t))). \quad (28)$$

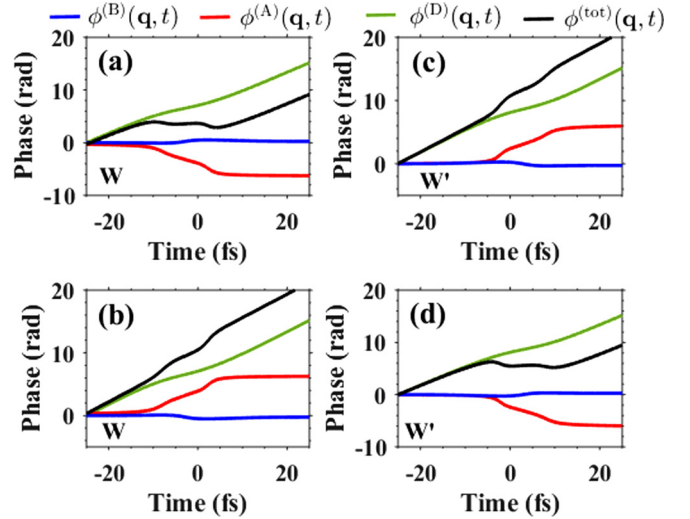


FIG. 4. Phases $\phi_{cv}^{(tot)}(\mathbf{q}, t)$, $\phi_{cv}^{(B)}(\mathbf{q}, t)$, $\phi_{cv}^{(A)}(\mathbf{q}, t)$, and $\phi_{cv}^{(D)}(\mathbf{q}, t)$ for different initial wave vectors in the vicinity of the separatrix. The initial wave vectors (q_x, q_y, q_z) are (a) $(-0.07, -0.06, -0.02)$, (b) $(-0.07, -0.06, 0.02)$, (c) $(0.07, -0.06, -0.02)$, (d) $(0.07, -0.06, 0.02)$. The amplitude of the pulse is $F_0 = 3$ mV/ \AA and it is left-hand circularly polarized.

Since $|\mathcal{A}_{cv}[\mathbf{k}(\mathbf{q}, t)]\mathbf{n}(t)|$ is a smooth function of time, the residual CB population [Eq. (26)] is determined by oscillating phase factor $\exp[i\phi_{cv}^{(tot)}(\mathbf{q}, t)]$ and the topological resonance occurs when the total phase is stationary, i.e., the topological phase, which is the combination of the geometric phase and the phase of the dipole matrix element, and the dynamic phase cancel each other.

Figure 3 shows the residual CB population distribution at $k_z = \pm 0.02$ $1/\text{\AA}$ induced by a circularly polarized pulse. The topological resonance, which manifests itself as a large CB population, can be explained by Fig. 4, where the corresponding phases $\phi_{cv}^{(A)}(\mathbf{q}, t)$, $\phi_{cv}^{(B)}(\mathbf{q}, t)$, $\phi_{cv}^{(D)}(\mathbf{q}, t)$, and $\phi_{cv}^{(tot)}(\mathbf{q}, t)$ are shown.

Since the magnitude of the interband coupling is the strongest near the Weyl points, which corresponds to $t = 0$ in Fig. 4, then we need to study the behavior of the total phase at t close to zero. For a given Weyl point, the phases $\phi_{cv}^{(A)}(\mathbf{q}, t)$ and $\phi_{cv}^{(B)}(\mathbf{q}, t)$ have opposite signs. Figures 4(a) and 4(b) show the different phases for a point near the W point for $k_z = -0.02$ $1/\text{\AA}$ and $k_z = 0.02$ $1/\text{\AA}$, respectively. The topological resonance is determined by behavior of the total phase $\phi_{cv}^{(tot)}(\mathbf{q}, t)$, around $t = 0$ fs. The total phase is almost constant for $k_z = -0.02$ $1/\text{\AA}$, and has strong time dependence for $k_z = 0.02$ $1/\text{\AA}$. Thus, the topological resonance results in large CB population for the W point at $k_z = -0.02$ $1/\text{\AA}$ while the CB population is relatively small for the W point at $k_z = 0.02$ $1/\text{\AA}$ plane. Opposite, for the W' point, the total phase is almost constant around $t = 0$ fs for $k_z = 0.02$ $1/\text{\AA}$, which results in corresponding large CB population [see Figs. 4(c) and 4(d)].

In Fig. 5, we show the CB population of four different Weyl semimetals type I as a function of k_x and k_y for $k_z = -0.02$ ($1/\text{\AA}$) after a single-oscillation left-handed circularly polarized pulse. The field amplitude of the pulse is $F_0 = 3$ mV/ \AA ,

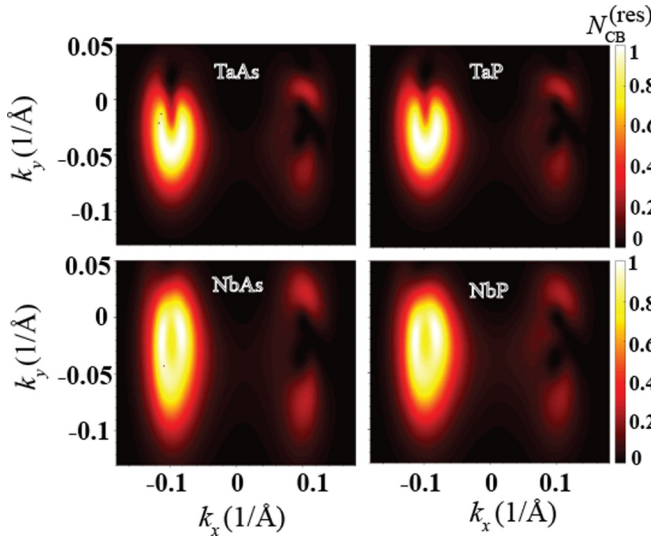


FIG. 5. Residual CB population distribution in the reciprocal space as a function of (k_x, k_y) for $k_z = -0.02$ ($1/\text{\AA}$) for TaAs, TaP, NbAs, NbP after a single-oscillation left-handed circularly polarized pulse. The pulse with the field amplitude $F_0 = 3$ mV/ \AA propagates along the z direction.

and the pulse propagates along the z direction. TaAs, TaP, NbAs, and NbP have the same body-centered tetragonal structure with different lattice parameters and different mean velocities at Weyl points [22]. The results show that the effect of topological resonance is present in all cases, regardless of their different parameters, and this is due to the fact that such effect mainly depends on the large Berry curvature at Weyl points at Weyl semimetals and it does not depend on the parameters of the Hamiltonian.

In addition, the total CB population as a function of time for TaAs, TaP, NbAs, and NbP is illustrated in Fig. 6. The results show that the total conduction band population of TaAs

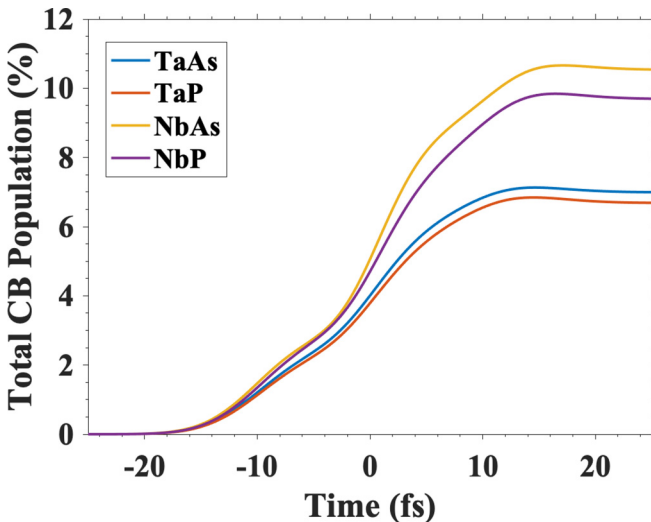


FIG. 6. Total conduction band population as a function of time for TaAs, TaP, NbAs, NbP for a single-oscillation left-handed circularly polarized pulse. The field amplitude is $F_0 = 3$ mV/ \AA .

and TaP is almost the same, which is due to the fact that the parameters of Hamiltonian (2) for TaAs and TaP are similar, and it is smaller than the conduction band population of NbAs and NbP.

The response of Weyl semimetals to an ultrafast circularly polarized optical pulse is the same as what was predicted for gapped graphene. In the case of gapped graphene, the right-hand circularly polarized pulse mostly populates the K valley while the CB population at the K' valley is small [18].

2. Type II Weyl semimetals

The type II Weyl semimetals are characterized by strong tilting of its energy dispersion near the Weyl points. As a result of such tilting, there are regions near the Weyl points where there are only VB states or only CB states. In terms of application to ultrafast electron dynamics in these regions, the interband coupling becomes effectively intraband coupling, i.e., at the same reciprocal vector two VB states (or two CB states) at different energies but with the same wave vector are coupled by the optical pulse. Such regions do not contribute to the topological resonance. As a result, for the type II Weyl semimetals we should expect suppression of effects related to the topological resonance.

To illustrate the ultrafast electron dynamics in type II Weyl semimetals, we consider a simple model of type II Weyl materials, which is described by the following Hamiltonian:

$$\mathcal{H}_0(\mathbf{k}) = A(\mathbf{k})\sigma_0 + B(\mathbf{k})\sigma_z + C(\mathbf{k})\sigma_x + D(\mathbf{k})\sigma_y, \quad (29)$$

where $\mathbf{k} = (k_x, k_y, k_z)$ is a vector of the reciprocal space, $\sigma_x, \sigma_y, \sigma_z$ are Pauli matrices, and $A(\mathbf{k}), B(\mathbf{k}), C(\mathbf{k})$, and $D(\mathbf{k})$ are given by the expressions

$$\begin{aligned} A(\mathbf{k}) &= t_1 \sin(k_y a) + t_2 \sin(2k_y a), & B(\mathbf{k}) &= \sin(k_y a), \\ C(\mathbf{k}) &= 1 - \cos(k_x a) - \cos(k_z a), & D(\mathbf{k}) &= \sin(k_z a), \end{aligned} \quad (30)$$

where $t_1 = -0.8, t_2 = -0.6, a = 7 \text{\AA}$, and σ_0 is the 2×2 unit matrix [28]. The corresponding energy dispersion is given by the expression

$$\begin{aligned} E_c(\mathbf{k}) &= A(\mathbf{k}) + \sqrt{B^2(\mathbf{k}) + C^2(\mathbf{k}) + D^2(\mathbf{k})}, \\ E_v(\mathbf{k}) &= A(\mathbf{k}) - \sqrt{B^2(\mathbf{k}) + C^2(\mathbf{k}) + D^2(\mathbf{k})}, \end{aligned} \quad (31)$$

where c and v stand for the CB and VB, respectively. The energy dispersion is shown in Fig. 7.

We apply a circularly polarized optical pulse [see Eq. (25)], which has the same profile as for the type I Weyl semimetals. The residual CB population is shown in Figs. 8 and 9. For $k_z = 0$, the CB population distribution is symmetric with respect to the k_y axis and has maxima near the Weyl points, which is similar to what we see in the type I Weyl semimetals. At the same time, while for type I Weyl semimetals the CB population distribution has a single maximum without any internal structure near each Weyl point, for type II Weyl semimetals the CB population distribution shows interference pattern with local maxima and minima (see Fig. 8). This is due to the fact that near each Weyl point of type II Weyl semimetals, there are regions with pure intraband dynamics.

For $k_z \neq 0$ (see Fig. 9), we can clearly see that CB population distribution is different around two Weyl points, which,

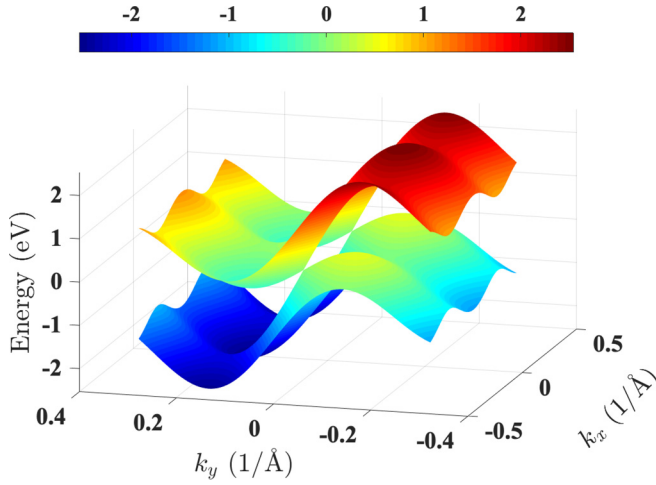


FIG. 7. Energy dispersion of type II Weyl semimetals as a function of k_x and k_y for $k_z = 0$.

similar to type I Weyl semimetals, is due to topological resonance. For type II Weyl semimetals, this difference is less pronounced than for type I materials. The reason for this is that the topological resonance occurs due to accumulation of the topological phase, which comes from the interband dynamics. For type II Weyl semimetals, in part of the region around the Weyl points the interband dynamics transforms into intraband dynamics, which finally results in suppression of the topological resonance.

B. Two-cycle circularly polarized pulse

We consider the response of the Weyl semimetal to a circularly polarized pulse consisting of two cycles. The pulse is incident normally on the system along the z direction and has

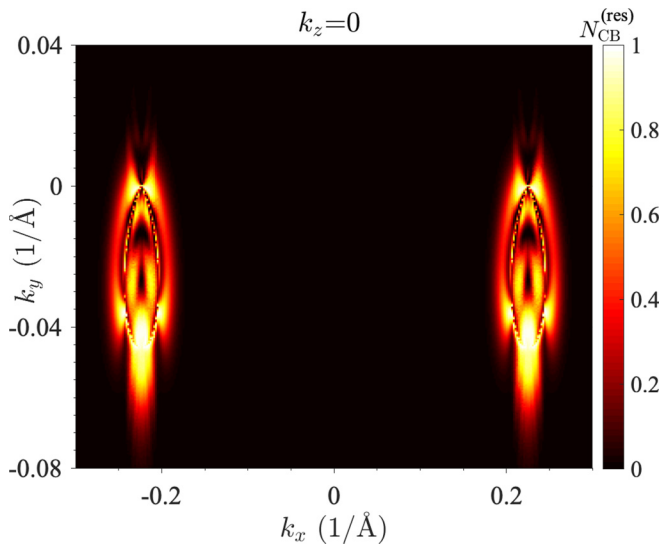


FIG. 8. Residual CB population distribution in the reciprocal space as a function of (k_x, k_y) for $k_z = 0$ for type II Weyl semimetals. The left-handed circularly polarized pulse propagates along the z direction and the field amplitude is $F_0 = 3$ mV/Å.

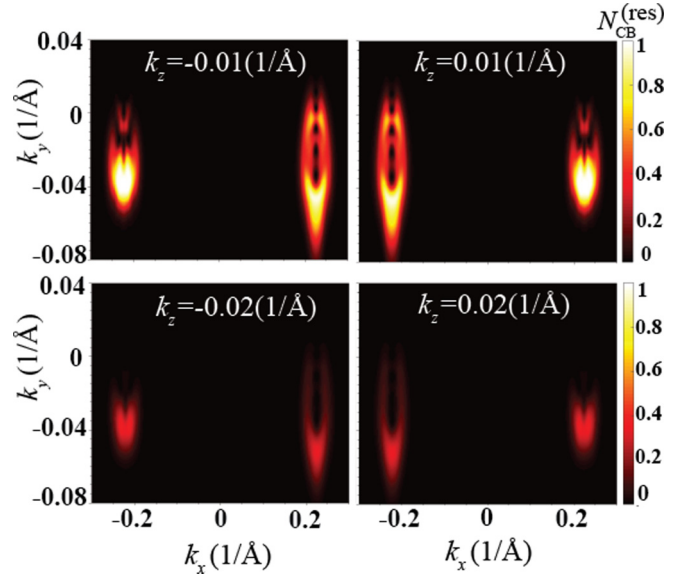


FIG. 9. Residual CB population distribution in the reciprocal space as a function of (k_x, k_y) for nonzero k_z for type II Weyl semimetals. The left-handed circularly polarized pulse propagates along the z direction and the field amplitude is $F_0 = 3$ mV/Å.

the following profile:

$$F_x(t) = F_0 \left[-e^{-u^2} (1 - 2u^2) \mp \alpha e^{-(u-u_0)^2} [1 - 2(u-u_0)^2] \right],$$

$$F_y(t) = 2F_0 \left[ue^{-u^2} + \alpha(u-u_0)e^{-(u-u_0)^2} \right]. \quad (32)$$

Here, \mp sign determines the handedness of the second cycle of the pulse relative to the handedness of the first cycle. Here the minus sign corresponds to the same handedness of two cycles, while the plus sign corresponds to the opposite handedness of two cycles. The amplitude of the first pulse cycle is $F_0 = 3$ mV/Å, while the amplitude of the second cycle is αF_0 , where $\alpha = 0.75$ in Figs. 10 and 11 and $\alpha = 1$ in Figs. 12 and 13. The duration of a single cycle of the pulse is $\tau = 10$ fs and the time interval between the cycles is $t_0 = 50$ fs, where $u_0 = t_0/\tau$.

The CB population distribution in the k_x - k_y plane is shown in Fig. (10) for $k_z = 0$ and for two optical cycles of opposite handedness. The results clearly show that the distribution is highly chiral at both Weyl points and is also characterized by interference fringes. The origin of such interference is a double passage by an electron of the region close to the Weyl points. Namely, at the end of the first cycle of the pulse, $t \approx 25$ (fs), the CB population distribution has maximum along the corresponding separatrix (see Figs. 2 and 3), but does not produce any interference fringes. Then, during the second cycle of the pulse, whose circularity is opposite of the circularity of the first cycle, electron passes through the Weyl point the second time resulting in the interference pattern. Such interference occurs because of highly localized nature of the interband dipole coupling, which has sharp maximum at the Weyl points, and because for a two-cycle pulse there are two amplitudes that determine the transfer of an electron from the valence band to the conduction band. Here, the first amplitude corresponds to the electron transfer from VB to CB during the first cycle, while the second amplitude corresponds

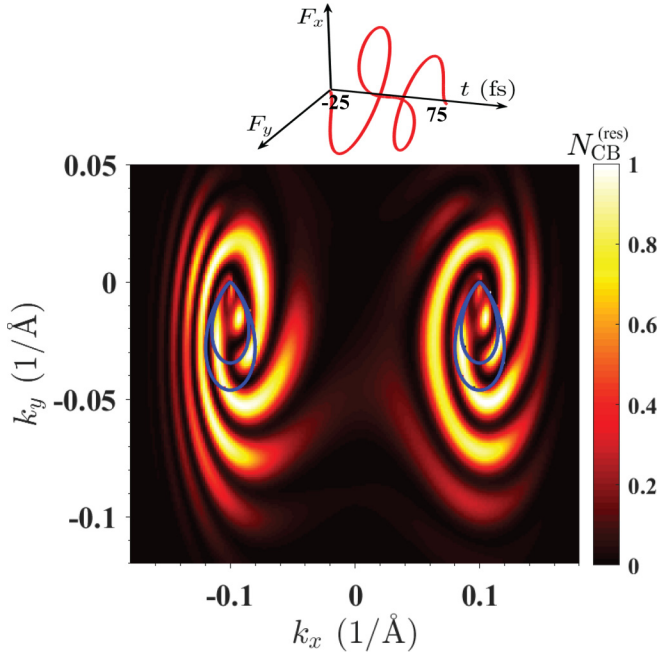


FIG. 10. Residual CB population distribution in the reciprocal space as a function of (k_x, k_y) at $k_z = 0$, after a two-cycle optical pulse. Here, the first cycle of the pulse is right-handed circularly polarized with the amplitude of $F_0 = 3 \text{ mV/\AA}$, and the second cycle is left-handed circularly polarized with the amplitude of $0.75F_0$. The separatrix corresponding to two cycles of pulses is shown by a solid blue line.

to the electron transfer from VB to CB during the second cycle. The phase, both the dynamic and topological, accumulated between these two transfers determines the interference pattern in the CB population distribution. This interferometer does not need an external reference source and, therefore, is self-referenced.

The results for two-cycle pulse, illustrated in Fig. 10, show that the CB population distributions are different for two Weyl points, while they are the same for one-cycle pulse. Such difference is due to intrinsic chirality of electron states at the Weyl points.

The results shown in Fig. 10 correspond to $k_z = 0$ when the interband dipole matrix element is highly localized at the Weyl points and there is no topological resonance during the

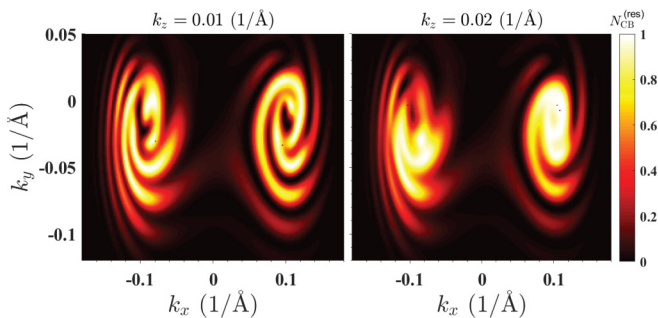


FIG. 11. Residual CB population as a function of (k_x, k_y) for two nonzero values of k_z . The profile of the pulse is the same as the one in Fig. 10.

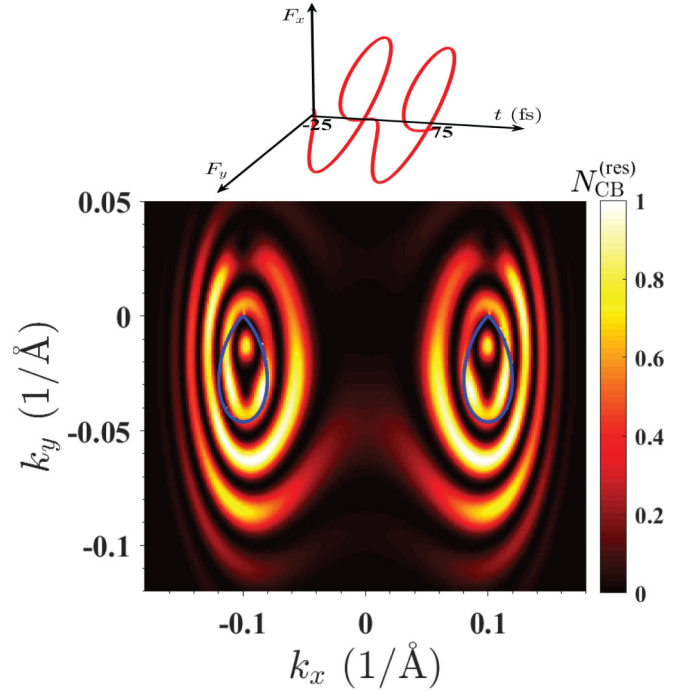


FIG. 12. Residual CB population as a function of (k_x, k_y) at $k_z = 0$ after a two-cycle optical pulse. The two cycles have the same circular polarization. The amplitude of the electric field for both cycles is $F_0 = 3 \text{ mV/\AA}$. The separatrix is shown as a blue line. The inset shows the profile of two-cycle optical pulse.

pulse. For the cross sections with $k_z \neq 0$, the electron system behaves similar to gapped graphene with well-developed topological resonance and broaden interband coupling. The corresponding results for a two-cycle pulse is shown in Fig. 11. The results clearly show that with increasing k_z the interference fringes become smeared. This is mainly related to the fact that for two-cycle pulse, which consists of two cycles with opposite handedness, the topological resonance, for a given Weyl point, occurs only for one of the cycles. As a

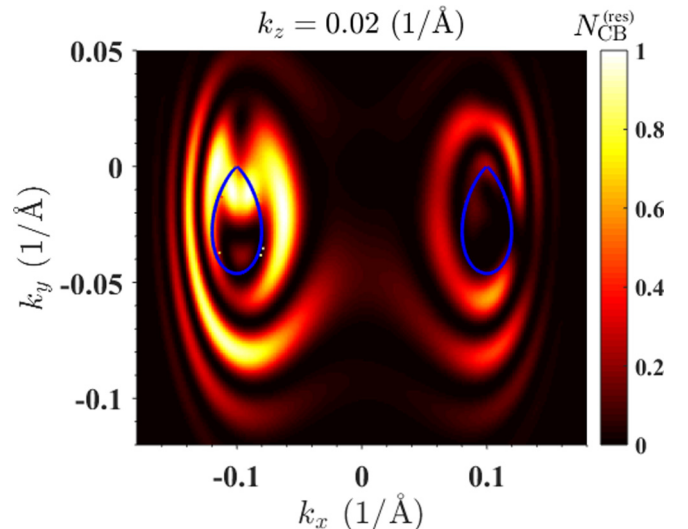


FIG. 13. The same as Fig. 12, but for $k_z = 0.02 (1/\text{\AA})$.

result, one of the amplitudes that determines CB-VB mixing during the two-cycle pulse becomes small compared to the other one, which finally smears the interference pattern. For example, in Fig. 11, the first cycle of the pulse has counter-clockwise polarization and it populates the W point, while the second cycle of the pulse has clockwise polarization and populates mainly the W' point.

The CB population distribution for two-cycle pulse with the same circular polarization and the same amplitude ($\alpha = 1$) for two cycles is shown in Figs. 12 and 13. For $k_z = 0$ (see Fig. 12), when the system is similar to pristine graphene, the CB population distributions at two Weyl points are the mirror image of each other (with respect to the k_y - k_z plane). The interference fringes in this case are mostly parallel to the separatrix, which is shown by blue line in the figure. This is due to the fact that the time between the first and the second passages by an electron of the Weyl points is large and is almost the same for all points on a given line parallel to the separatrix. This results in strong dephasing and the same interference conditions along such lines.

For nonzero k_z , the system is equivalent to gapped graphene with well-pronounced topological resonance. For two-cycle optical pulse with the same handedness for both cycles, the topological resonance is realized only for one of the Weyl points for both cycles. In this case, the whole CB population distribution becomes strongly suppressed for one of the Weyl points. This behavior is clearly illustrated in Fig. 13, where the whole CB population of Weyl point W' is suppressed.

IV. CONCLUSION

The ultrafast interband electron dynamics in Weyl semimetals is controlled by competition between the dynamic phase and the topological phase, which occurs in the field of a circularly polarized femtosecond long optical pulse. When these two phases cancel each other, the system exhibits the topological resonance, which results in large residual conduction band population. For Weyl semimetals, for the pulse

propagating along, for example, the z direction, the topological resonance results in predominant CB population of the region in the reciprocal space near one of the Weyl points, say W , for $k_z < 0$ and the region near the other Weyl point, W' , for $k_z > 0$. Exactly at $k_z = 0$ conduction bands at both Weyl points are equally populated. The reason for such behavior is that for each cross section $k_z = \text{const}$, the Weyl semimetals behave as a 2D gapped graphene system with the gap that is proportional to k_z . Since the strength of the topological resonance in gapped graphene system increases with the magnitude of the band gap and manifests itself in predominant population of one of the valleys, then similar features of topological resonance are visible in 3D Weyl semimetals. At the same time, the dynamics of Weyl semimetals in circularly polarized pulse can be used to study the properties of topological resonance, i.e., its dependence on the band gap and energy dispersion of the material, and profile and intensity of the optical pulse.

Furthermore, employing a two-cycle circularly polarized pulse causes the formation of interferogram in the conduction band population distribution in the reciprocal space. Such distribution is also highly chiral for the two Weyl nodes and illustrates the intrinsic chirality of the Weyl points. The interferogram also depends on the strength of the topological resonance and can be used to study the properties of the topological resonance in topological materials.

ACKNOWLEDGMENTS

Major funding was provided by Grant No. DE-SC0007043 from the Materials Sciences and Engineering Division of the Office of the Basic Energy Sciences, Office of Science, U.S. Department of Energy. Numerical simulations were performed using support by Grant No. DE-FG02-01ER15213 from the Chemical Sciences, Biosciences and Geosciences Division, Office of Basic Energy Sciences, Office of Science, U.S. Department of Energy. The work of V.A. was supported by NSF EFRI NewLAW Grant No. EFMA-17 41691. Support for F.N. came from MURI Grant No. FA9550-15-1-0037 from the U.S. Air Force Office of Scientific Research.

-
- [1] G. Wachter, C. Lemell, J. Burgdörfer, S. A. Sato, X.-M. Tong, and K. Yabana, *Ab Initio* Simulation of Electrical Currents Induced by Ultrafast Laser Excitation of Dielectric Materials, *Phys. Rev. Lett.* **113**, 087401 (2014).
 - [2] F. Nematollahi, V. Apalkov, and M. I. Stockman, Phosphorene in ultrafast laser field, *Phys. Rev. B* **97**, 035407 (2018).
 - [3] G. Su, F. Wang, L. Jiang, X. Zhang, X. Su, L. Qu, and Y. Lu, Ultrafast response of dielectric properties of monolayer phosphorene to femtosecond laser, *J. Appl. Phys.* **121**, 173105 (2017).
 - [4] F. Nematollahi, V. Apalkov, and M. I. Stockman, Weyl semimetals in circularly-polarized ultrafast laser field, in *Frontiers in Ultrafast Optics: Biomedical, Scientific, and Industrial Applications XIX*, Vol. 10908 (SPIE, International Society for Optics and Photonics, Bellingham, WA, 2019), p. 1090803.
 - [5] S. A. O. Motlagh, J.-S. Wu, V. Apalkov, and M. I. Stockman, Femtosecond valley polarization and topological resonances in transition metal dichalcogenides, *Phys. Rev. B* **98**, 081406(R) (2018).
 - [6] S. A. O. Motlagh, F. Nematollahi, A. Mitra, A. J. Zafar, V. Apalkov, and M. I. Stockman, Ultrafast optical currents in gapped graphene, *J. Phys.: Condens. Matter* **32**, 065305 (2019).
 - [7] S. M. Young, S. Zaheer, J. C. Y. Teo, C. L. Kane, E. J. Mele, and A. M. Rappe, Dirac Semimetal in Three Dimensions, *Phys. Rev. Lett.* **108**, 140405 (2012).
 - [8] F. Koppens, T. Mueller, P. Avouris, A. Ferrari, M. Vitiello, and M. Polini, Photodetectors based on graphene, other two-dimensional materials and hybrid systems, *Nat. Nanotechnol.* **9**, 780 (2014).
 - [9] K. S. Novoselov, V. I. Fal'ko, L. Colombo, P. R. Gellert, M. G. Schwab, and K. Kim, A roadmap for graphene, *Nature (London)* **490**, 192 (2012).
 - [10] A. A. Burkov and L. Balents, Weyl Semimetal in A Topological Insulator Multilayer, *Phys. Rev. Lett.* **107**, 127205 (2011).

- [11] G. B. Halász and L. Balents, Time-reversal invariant realization of the weyl semimetal phase, *Phys. Rev. B* **85**, 035103 (2012).
- [12] H. B. Nielsen and M. Ninomiya, Absence of neutrinos on a lattice:(i). proof by homotopy theory, *Nucl. Phys. B* **185**, 20 (1981).
- [13] A. A. Zyuzin and A. Y. Zyuzin, Chiral anomaly and second-harmonic generation in weyl semimetals, *Phys. Rev. B* **95**, 085127 (2017).
- [14] I. Sodemann and L. Fu, Quantum Nonlinear Hall Effect Induced by Berry Curvature Dipole in Time-Reversal Invariant Materials, *Phys. Rev. Lett.* **115**, 216806 (2015).
- [15] Q. Ma, S.-Y. Xu, C.-K. Chan, C.-L. Zhang, G. Chang, Y. Lin, W. Xie, T. Palacios, H. Lin, S. Jia *et al.*, Direct optical detection of weyl fermion chirality in a topological semimetal, *Nat. Phys.* **13**, 842 (2017).
- [16] R. Yu, H. Weng, Z. Fang, H. Ding, and X. Dai, Determining the chirality of weyl fermions from circular dichroism spectra in time-dependent angle-resolved photoemission, *Phys. Rev. B* **93**, 205133 (2016).
- [17] F. Nematollahi, S. A. O. Motlagh, V. Apalkov, and M. I. Stockman, Weyl semimetals in ultrafast laser fields, *Phys. Rev. B* **99**, 245409 (2019).
- [18] S. A. O. Motlagh, F. Nematollahi, V. Apalkov, and M. I. Stockman, Topological resonance and single-optical-cycle valley polarization in gapped graphene, *Phys. Rev. B* **100**, 115431 (2019).
- [19] M. Z. Hasan, S.-Y. Xu, I. Belopolski, and S.-M. Huang, Discovery of weyl fermion semimetals and topological fermi arc states, *Annu. Rev. Condens. Matter Phys.* **8**, 289 (2017).
- [20] J. Murray, J. Taylor, L. Calvert, Y. Wang, E. Gabe, and J. Despault, Phase relationships and thermodynamics of refractory metal pnictides: The metal-rich tantalum arsenides, *J. Less-Common Met.* **46**, 311 (1976).
- [21] B. Q. Lv, H. M. Weng, B. B. Fu, X. P. Wang, H. Miao, J. Ma, P. Richard, X. C. Huang, L. X. Zhao, G. F. Chen, Z. Fang, X. Dai, T. Qian, and H. Ding, Experimental Discovery of Weyl Semimetal TaAs, *Phys. Rev. X* **5**, 031013 (2015).
- [22] C.-C. Lee, S.-Y. Xu, S.-M. Huang, D. S. Sanchez, I. Belopolski, G. Chang, G. Bian, N. Alidoust, H. Zheng, M. Neupane *et al.*, Fermi surface interconnectivity and topology in weyl fermion semimetals TaAs, TaP, NbAs, and NbP, *Phys. Rev. B* **92**, 235104 (2015).
- [23] F. Bloch, Über die quantenmechanik der elektronen in kristallgittern, *Z. Phys.* **52**, 555 (1929).
- [24] W. Houston, Acceleration of electrons in a crystal lattice, *Phys. Rev.* **57**, 184 (1940).
- [25] M. V. Berry, Quantal phase factors accompanying adiabatic changes, *Proc. R. Soc. London A* **392**, 45 (1984).
- [26] D. Xiao, M.-C. Chang, and Q. Niu, Berry phase effects on electronic properties, *Rev. Mod. Phys.* **82**, 1959 (2010).
- [27] H. K. Kelardeh, V. Apalkov, and M. I. Stockman, Attosecond strong-field interferometry in graphene: Chirality, singularity, and berry phase, *Phys. Rev. B* **93**, 155434 (2016).
- [28] M. Trescher, Tilted Weyl Semimetals, Ph.D. thesis, Freie Universität Berlin, 2018.